PHYSICAL REVIEW B **95**, 165426 (2017)

Multimode directionality in all-dielectric metasurfaces

Yuanqing Yang,[1] Andrey E. Miroshnichenko,[2] Sarah V. Kostinski,[2,3] Mikhail Odit,[4] Polina Kapitanova,[4]
Min Qiu,[1,*] and Yuri S. Kivshar[2,4,†]
[1]*State Key Laboratory of Modern Optical Instrumentation, College of Optical Science and Engineering,*
Zhejiang University, Hangzhou 310027, China
[2]*Nonlinear Physics Center, Research School of Physics and Engineering, Australian National University, Canberra ACT 2601, Australia*
[3]*Department of Physics, Harvard University, Cambridge, Massachusetts 02138, USA*
[4]*Department of Nanophotonics and Metamaterials, ITMO University, St. Petersburg 197101, Russia*

(Received 16 September 2016; revised manuscript received 23 March 2017; published 18 April 2017)

We demonstrate that spectrally diverse multiple magnetic dipole resonances can be excited in all-dielectric structures lacking rotational symmetry, in contrast to conventionally used spheres, disks, or spheroids. Such multiple magnetic resonances arise from hybrid Mie-Fabry-Perot modes, and can constructively interfere with induced electric dipole moments, thereby leading to novel multifrequency unidirectional scattering. Here we focus on elongated dielectric nanobars, whose magnetic resonances can be spectrally tuned by their aspect ratios. Based on our theoretical results, we suggest all-dielectric multimode metasurfaces and verify them in proof-of-principle microwave experiments. We also believe that the demonstrated property of multimode directionality is largely responsible for the best efficiency of all-dielectric metasurfaces that were recently shown to operate across multiple telecom bands.

DOI: 10.1103/PhysRevB.95.165426

I. INTRODUCTION

Modern nanophotonics aims to efficiently manipulate light at the nanoscale, with applications ranging from near-field microscopy and integrated optoelectronics to biomedical science [1]. Recent decades have witnessed a growing research interest in the study of *plasmonic nanoparticles* made of gold or silver, recognized for their outstanding ability to squeeze light into subwavelength volumes via surface-plasmon resonances. The resonant optical plasmonic modes supported by metallic structures endow them with an ability to manipulate light at subwavelength scales. These optical resonances are highly dependent on the choice of the structure's material and geometry, allowing for further manipulations. Various types of photonic devices based on plasmonic nanoparticles have thus been demonstrated [1–5]. However, their overall functionalities and performance are severely affected by high intrinsic losses in metals. When larger amounts of metals are involved in complex plasmonic structures such as metamaterials or metadevices [6–8], the loss problem is exacerbated and hinders their scalability for practical use.

Whereas new materials with improved plasmonic properties have been proposed, there has also been a growing realization that the optical resonances of high-index resonant dielectric structures can facilitate light manipulation below the free-space diffraction limit with very low losses [9–26]. In contrast to plasmonic nanoparticles that are dominated by electric resonances, high-refractive-index dielectric nanoparticles have proven to support both *electric and magnetic* Mie-type dipole and multipole resonances, opening up new possibilities for designer photonic metadevices [9–18]. For example, by using an isolated magnetic dipole Mie resonance, a magnetic mirror can be realized [26]. While if we use a magnetic dipole that is spectrally overlapped with an electric dipole, these two dipole modes can satisfy the first Kerker condition [27] and constructively interfere with each other, leading to directional scattering and the realization of transparent Huygens' metasurfaces [9,10]. Therefore, how to fully exploit these intriguing optically induced electric and magnetic resonances becomes extremely crucial for realizing and functionalizing dielectric metasurfaces.

However, in all studied dielectric resonant structures presented so far, the geometry of dielectric nanoparticles is considered to be close to either spheres [11–13], spheroids/disks [14–16], cubes [17,18], or long rod [19,20] [see Figs. 1(a) and 1(c)], so the exact Mie solutions of the two- (2D) and three-dimensional (3D) scattering problems can be applied to analyze the scattering by such isotropic or symmetric nanostructures. These symmetric structures, as verified by Mie theory and associated multipole expansion, can support a series of different resonances, with first-order Mie resonance usually a *single* magnetic dipole mode, the second-order a *single* electric dipole, and subsequent higher-order electric and magnetic multipoles. By contrast, if we consider dielectric nanoparticles with broken rotational symmetry such as finite-size nanobars [see Fig. 1(b)], as we will show in the following, such asymmetric meta-atoms will not only introduce new physics into the classical Mie scattering problem but can also bring novel functionality to all-dielectric structures and metasurfaces.

In this paper, we focus on silicon nanobars with *a large aspect ratio* and demonstrate that such elongated nanostructures can support hybrid Mie-Fabry-Perot modes associated with *multiple* magnetic dipole resonances. These intriguing modes arise from the combination of conventional magnetic dipole modes excited in the transverse direction (*Mie resonances*) and the standing waves excited in the longitudinal direction (*Fabry-Perot cavity modes*). Moreover, just like single magnetic dipoles, such multiple magnetic dipole modes can also constructively interfere with induced electric dipoles, thereby

---

[*] minqiu@zju.edu.cn
[†] Yuri.Kivshar@anu.edu.au

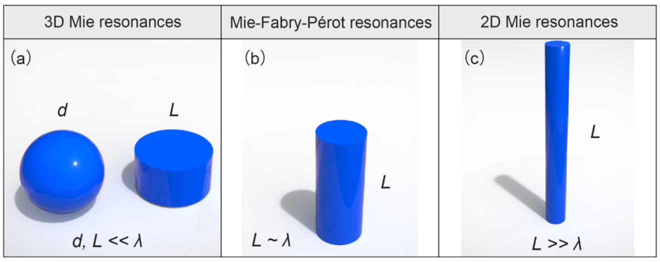

FIG. 1. Classes of all-dielectric meta-atoms: (a) Sphere and nanodisk with high refractive index described by the three-dimensional Mie scattering theory. Characteristic dimensions (d and L) are much smaller than the free-space wavelength λ. (b) Finite-size nanorod ($L \sim \lambda$) with a high aspect ratio supporting the hybrid Mie-Fabry-Perot as described in this work. (c) Long nanorod ($L \gg \lambda$) described by the two-dimensional Mie scattering theory.

leading to multifrequency directional scattering, characterized by multiple Kerker conditions. Based on our theoretical results, we further demonstrate novel all-dielectric Huygens' metasurfaces with spectrally diverse directionality verified in proof-of-principle microwave experiments. Due to the existence of multiple magnetic dipoles, such metasurfaces can work efficiently in both reflection and transmission modes and also achieve all four quadrants of electromagnetic responses: $\epsilon > 0$, $\mu > 0$; $\epsilon < 0$, $\mu > 0$; $\epsilon > 0$, $\mu < 0$; $\epsilon < 0$, $\mu > 0$, where ϵ and μ are electric permittivity and magnetic permeability, respectively. It is also worth noting that whereas there are some recent efforts on metasurfaces using dielectric building blocks with broken rotational symmetry [28–30], most designs do not directly rely on the resonances of single elements [10,28,29] and only fundamental electric and magnetic dipole modes have been studied [30]. Finally, we also argue that the operation of the recently demonstrated broadband all-dielectric metasurfaces [31] is largely due to the multiple magnetic multipole modes of the constituent elements in the form of tall dielectric rods, allowing the achievement of destructive interference in reflection over a large spectra bandwidth. Our findings are expected to provide a methodology to design broadband and multifunctional all-dielectric metadevices.

II. SCATTERING AND MULTIPOLE DECOMPOSITION

The schematic of a designed silicon nanobar is shown in Fig. 2(a). The geometric parameters are all different in three dimensions with $W = 110$ nm, $L_z = 220$ nm, and $L_y = 400$ nm. For comparison, we also introduce a symmetric silicon nanobar with $L_y = L_z = L = W = 400$ nm, as depicted in Fig. 2(b). Here we use 3D finite-difference time-domain (FDTD) simulations [32] and the Cartesian multipole analysis (see Appendix A) to calculate the response of the structures and identify the contributions from each multipole moment. The optical constants of silicon are taken from Palik's handbook [33] while the surrounding media is assumed to be air. The structures are illuminated by a normally incident plane wave with electric field along y direction.

Figures 2(c) and 2(d) represent the calculated scattering efficiency spectra and decomposed multipole contributions.

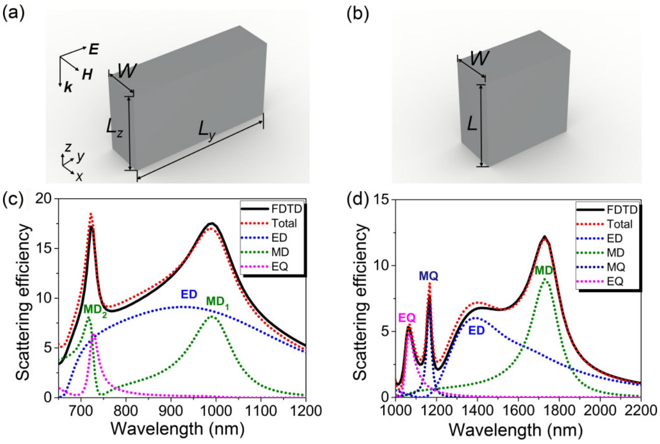

FIG. 2. (a), (b) Schematic diagrams of (a) an elongated ($W = 110$ nm, $L_y = 400$ nm, and $L_z = 220$ nm) and (b) a symmetric ($W = L = 400$ nm) silicon nanobar. (c), (d) Simulated scattering spectra (solid black line) and calculated multipole decompositions (total contributions: dotted red line, ED: dotted blue line, MD: dotted green line, EQ: dotted magenta line) of (c) the elongated and (d) symmetric nanobar, respectively.

The scattering efficiency Q_{eff} is defined as $Q_{\text{eff}} = Q_{\text{sca}}/Q_{\text{geo}}$, where Q_{sca} and Q_{geo} are scattering and geometrical cross sections of the particle, respectively. Here in our case, $Q_{\text{geo}} = W \times L_y$. For multipole expansion, we only consider the first four terms, namely, electric dipole (ED), magnetic dipole (MD), electric quadrupole (EQ), and magnetic quadrupole (MQ) modes. The scattering spectra obtained from the FDTD simulations (solid black line) and the multipole expansion (dotted red line) are in a good agreement with each other, indicating that higher-order multipoles are negligible in our case. At first glance, both scattering spectra of the nanobars have similar optical responses with two pronounced maxima [cf. dotted black curves in Figs. 2(c) and 2(d)]. However, through the multipole expansion, we reveal that the underlying contributions of each multipole moment to these peaks are *completely different*. For the symmetric nanobar, the peaks are attributed to the separated MD and ED resonant modes, as has been reported in many previous studies on all-dielectric spheres, disks, or cubes. By contrast, the first peak in the scattering spectrum of the elongated nanobar shows a resonance overlap of MD and ED, while the second peak arises from the second maximum in the magnetic dipole contribution, implying the existence of a second-mode magnetic dipole (MD_2), which has never been discussed or demonstrated before. We would also like to note that this MD_2 mode is essentially different from conventional MQ mode, which will be shown in the following section.

III. MULTIFREQUENCY DIRECTIONAL SCATTERING

To further illustrate the properties of the isotropic nanobar and especially the MD_2 mode, in Fig. 3 we plot the near- and far-field distributions at two peak wavelengths ($\lambda = 992$ nm and $\lambda = 721$ nm). For $\lambda = 992$ nm, the induced ED (parallel to the incident polarization, p_{y1}) and MD (m_{x1}) dominate the near-field profiles with very close amplitudes

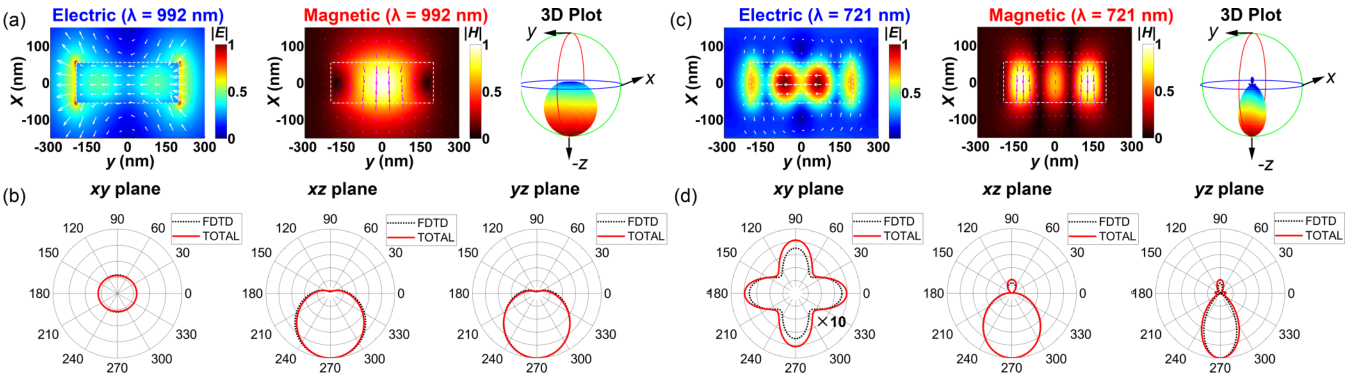

FIG. 3. (a), (c) Near-field distributions in the middle cut plane ($z = 0$) and 3D far-field scattering patterns of the nanobar at (a) $\lambda = 992$ nm and (c) $\lambda = 721$ nm, respectively. The colors represent normalized amplitudes of the electric and magnetic fields, and arrows show the field vectors. (b), (d) Simulated far-field scattering patterns (dotted black line) and calculated multipole radiation patterns (solid red line) at (b) $\lambda = 992$ nm and (d) $\lambda = 721$ nm, respectively. The patterns are normalized to the maximum scattering intensity in the far field.

($|p_{y1}| = 1.03 \times |m_{x1}|/c$, where c is the speed of light in vacuum) and a moderate phase difference ($\Delta\phi \sim 23^\circ$), making them approximately satisfy the first Kerker condition [27] and thus resulting in unidirectional forward scattering along z direction, as shown in Figs. 3(a) and 3(b). The simulated scattering patterns (dotted black lines) are also in an excellent accordance with the calculated radiation patterns from decomposed multipoles (solid red lines).

Figure 3(c) shows contrasting field distributions at $\lambda = 721$ nm. We observe that standing-wave patterns appear in both electric and magnetic fields, providing valuable insights into the nature of the MD_2 mode. The electric field is the superposition of a standing wave E_z and an induced ED mode (p_{y2}) in y direction, whereas the magnetic field is the consequence of a standing wave H_x along with an induced MD mode in x direction as well, leading to the appearance of the hybrid Mie-Fabry-Perot mode MD_2 (see Appendix B for theoretical standing-wave decompositions). In spite of the standing-wave pattern or fluctuations in the magnetic field distribution, the MD_2 mode still has a net magnetic dipole moment (m_{x2}) in $-x$ direction, just like the fundamental MD mode that we now call MD_1 mode. Interestingly, this magnetic dipole moment can also nearly satisfy the first Kerker condition with the electric dipole ($|p_{y2}| = 0.98 \times |m_{x2}|/c, \Delta\phi \sim 13^\circ$), thereby offering the novel behavior of multimode (multifrequency) unidirectional scattering (see Appendix C for theoretical explanations). This unique property is clearly shown in Fig. 3(d). We can find good agreement between the simulated and calculated angular patterns. Meanwhile, we should remember the existence of the EQ mode. Although it brings about small undesired backscattering, it also substantially narrows the scattering pattern and boosts the directivity. A front-to-back power ratio higher than 9 thus could be obtained in this case.

Besides the two well-defined maxima in the scattering spectrum, there is also a noticeable dip around $\lambda = 767$ nm [see in Fig. 2(c)], accompanied by a minimum near zero in the MD contribution, indicating that the contribution of the MD mode to the far field almost vanishes. This dip can be attributed to the cancellation of the induced magnetic dipoles which have opposite directions in the antinodes of the standing-wave pattern, mimicking a magnetic "dark mode." Specifically, the amplitude of the net magnetic dipole moment at $\lambda = 767$ nm is only $\sim$1/5 of that of the electric dipole moment, corresponding to $\sim$1/25 in the far-field contributions.

Since the MD_2 mode arises from a magnetic standing-wave pattern, one can intuitively expect a strong dependence of geometric parameters on the mode characteristics and further contributions to the scattering properties. In Figs. 4(a) and 4(c), we use two-dimensional color maps to show the impact of the geometric parameters W and L_y on the scattering spectra. With increasing length L_y and width W, we can see evident redshifts and the newly emerged higher-order Mie resonances. These redshifts and new Mie resonances, along with the Fabry-Perot resonances, can further lead to other multimode ED and MD besides the MD_2 mode. For instance, the scattering spectra for nanobars with $L_y = 1000$ nm and $W = 300$ nm, marked by the dashed black lines in the 2D color maps, show a fascinating property of triple-wavelength unidirectional scattering supported by an individual nanobar [Figs. 4(b) and 4(d)]. This is exactly due to the interferences of the multimode MD and

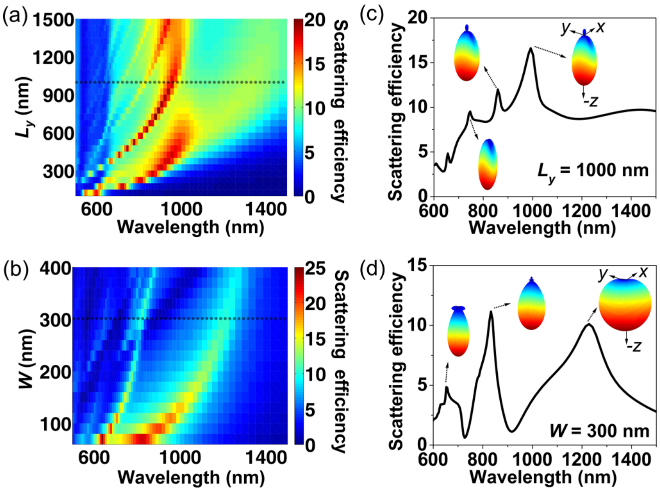

FIG. 4. Scattering efficiency spectra as a function of geometric parameters (a) L_y with fixed $W = 110$ nm and $L_z = 220$ nm, and (b) W with fixed $L_z = 220$ nm and $L_y = 400$ nm. (c), (d) Scattering spectrum for a nanobar with dimensions marked by the dashed lines in (a) and (b) correspondingly. The insets show the far-field unidirectional scattering patterns at different resonance wavelengths.

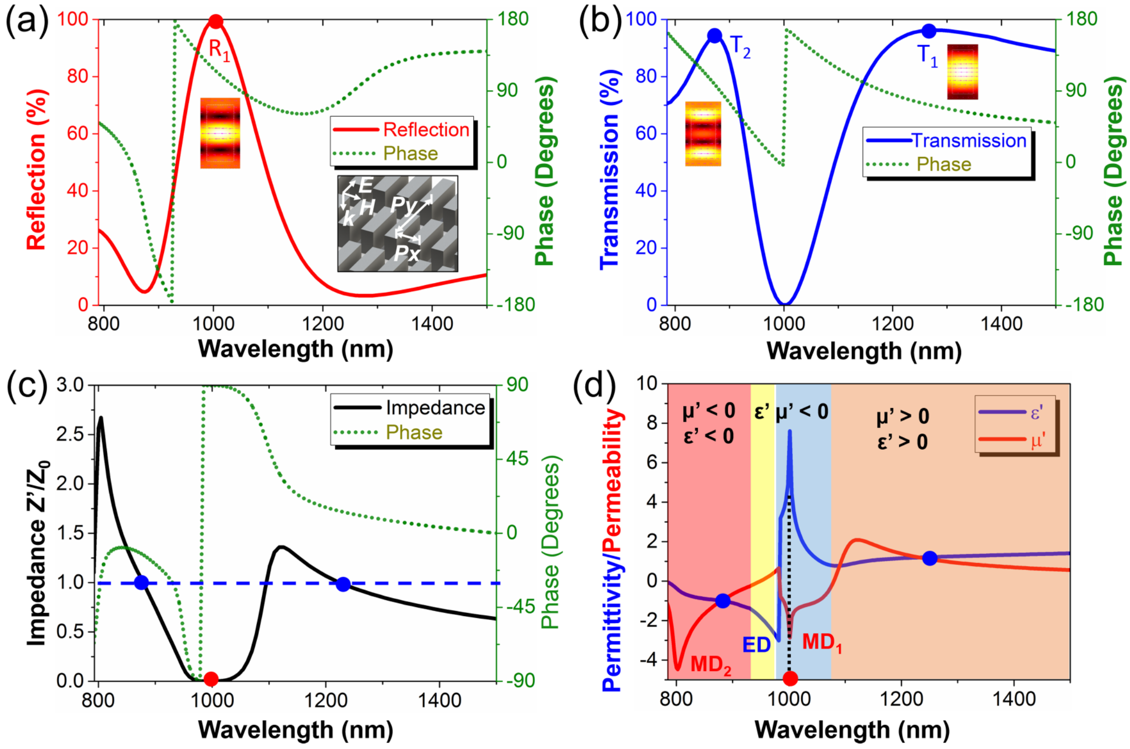

FIG. 5. (a), (b) Reflection and transmission spectra of the metasurface composed of the silicon nanobars shown in Fig. 2(a). The periodicities in x and y directions are 160 and 500 nm, respectively. Insets diagram the configuration and corresponding near-field magnetic distributions in the xy plane at R_1, T_1, and T_2 peak wavelengths. (c) Calculated impedance of the metasurface. The solid black line is the real value Z' of the impedance Z, which corresponds predominantly to radiation resistance. The green dotted line is the impedance phase. The blue dashed line indicates the impedance-matching condition $Z' = Z_0$. (d) Effective permittivity (blue) and permeability (red) of the metasurface obtained using S-parameter retrieval. ϵ' and μ' denote the real parts of ϵ and μ.

ED as well as other multipole moments excited inside the nanobars with increasing geometric parameters, accompanied by increasing-order Fabry-Perot modes. In particular, it can be seen that, the increase in L_y results in higher-mode MD while the increase in W brings about higher-mode ED (see Appendix D).

IV. MULTIMODE METASURFACES

Since the presented individual nanobars have proven to support multifrequency directional scattering, we expect that a metasurface composed of such nanobars can also have a multimode response. In Fig. 5 we plot reflection and transmission full spectra (intensity and phase) of such a metasurface. The inset diagrams the metasurface with $P_x =$ 160 nm and $P_y = 500$ nm (periodicities in x and y directions) on a glass substrate ($n_{\text{glass}} = 1.5$). One reflection peak R_1 and two transmission peaks T_1 and T_2 can be seen in the plots, indicating that our metasurface can function as either a perfect mirror or a transparent film at different wavelengths. At transmission peak T_1, the fundamental electric and magnetic dipole moments (ED_1 and MD_1) constructively interfere with each other and lead to the high transmission. While at the high reflection peak R_1, a standing-wave pattern appears and the magnetic dipole moment has an opposite direction to that at T_1. With the electric field kept in the same direction, this will lead to a reversal in the direction of power flow, i.e., changing from high transmission to high reflection. By contrast, at the second transmission peak T_2, the hybrid magnetic dipole moment once again has the same direction as that in T_1, thereby resulting in a second high transmission peak. This phase-flipping phenomenon of the magnetic dipoles and associated multimode high transmission are directly due to the emergence of MD_2 modes. Moreover, these multiple resonant modes also enable both reflected and transmitted light to experience significant phase changes with maintained high efficiency. The abrupt phase changes arising from the resonances can be easily tuned by varying the sizes of the nanostructures, which can be further used in the implementation of perfect reflectors, magnetic mirrors, or gradient metasurfaces [9,10]. Compared to previous studies where metasurfaces can only work in reflection or transmission modes, our metasurface makes it possible to control both reflected and transmitted light, which can remarkably extend the functionality of metasurfaces.

Figure 5(c) shows the calculated impedance of the metasurface. The two transmission peaks T_1 and T_2 correspond well to the impedance-matched points while reflection peak R_1 corresponds to a largely mismatched point where the wave impedance becomes predominantly imaginary. A striking flip of the impedance phase also occurs around 990 nm from $+90^\circ$ to -90°, indicating the metasurface switching fast from a magnetic conductor to an electric conductor [17].

To better understand the optical response of the metasurface, we also adopted a standard S-parameter retrieval method [34] to compute the effective permittivity and permeability, as shown in Fig. 5(d). Two notable magnetic resonances

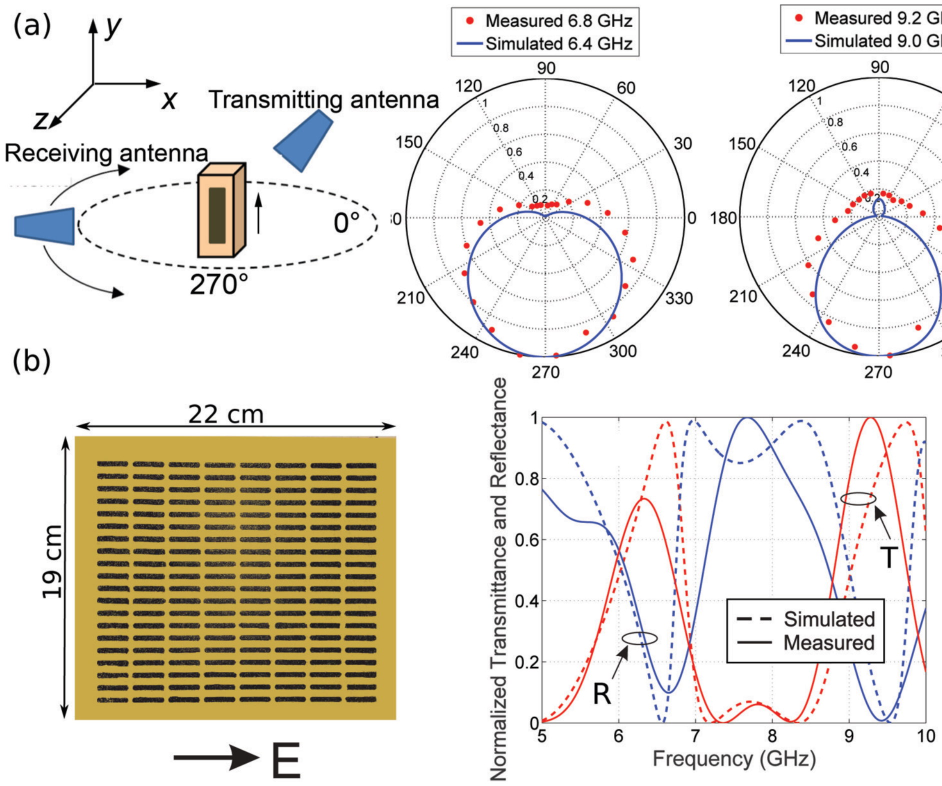

FIG. 6. (a) Dielectric bar scatter. Left: A sketch of the experimental setup to measure the radiation pattern of the single scatter with the dimensions $W = 0.5$ cm, $L_y = 1.8$ cm, and $L_z = 1.5$ cm. Right: Experimentally measured (red dots) and CST numerically simulated (solid curves) radiation patterns for the Kerker conditions. (b) Dielectric metasurface. Left: photograph of the fabricated multimode Huygens' metasurface composed of silicon dielectric bars with the dimensions $W = 0.5$ cm, $L_y = 1.8$ cm, and $L_z = 1.5$ cm placed with the periods $P_x = 0.9$ cm and $P_y = 2.7$ cm. Right: Experimentally measured (solid curves) and CST numerically simulated (dashed curves) reflection and transmission spectra magnitudes of the multimode Huygens' metasurface.

and one electric resonance could be observed. Combing the corresponding near-field distributions, it is easy to verify the existences of the ED, MD_1, and MD_2 mode induced in the metasurface. The spectral positions of these modes are different from those induced in the individual nanobar because of the substrate effect and the mutual interaction. Two intersections between the plots of permittivity and permeability indicate the impedance-matched points and the fulfillment of the Kerker condition. The first transmission T1 appears at the tails of the fundamental ED and MD_1 resonances, showing an off-resonant directionality. In this region ($\lambda > 1080$ nm), the permittivity and permeability of the metasurfaces are both above zero, which means the overall response of the metasurface is similar to conventional dielectric materials. However, for shorter wavelengths, the electric and magnetic resonances lead to distinct phenomena. The MD_1 mode makes the metasurface function as a magnetic mirror which has a negative permeability ($\mu < 0$) while the ED mode enables the metasurface to function as an electric mirror with a negative permittivity ($\epsilon < 0$). More interestingly, these two contrasting behaviors can be switched to each other very fast since the ED and MD_1 modes are spectrally very close to each other. This is also in good accordance with the impedance phase flip occurring at 980 nm. Another fascinating feature of the metasurface is its negative refractive index ($\epsilon < 0$, $\mu < 0$) attributed to the MD_2 and the ED modes for $\lambda < 950$ nm. In this region, the constructive interference of the MD_2 and ED modes happens in both of their resonance regimes, resulting in an efficient Huygens source with negative permittivity and permeability. Therefore, our metasurface can support all four quadrants of possible optical responses, which can bring various unexplored possibilities and functionalities.

To verify the proposed concept experimentally, the silicon nanobars are scaled up to the microwave frequency range. Here we employ full-scale numerical simulations [35] to optimize bar scatterers and use Eccostock HiK ceramic powder (permittivity $\varepsilon = 10$ and loss tangent $\tan\theta = 0.0007$) as the high-index dielectric material to mimic silicon nanobars in the microwave region.

First, we study experimentally the scattering from a single bar scatter in an anechoic chamber. The experimental setup is sketched in Fig. 6(a). To perform a plane-wave excitation and to receive the scattered signal, we utilized a pair of identical rectangular linearly polarized wideband horn antennas (operational range 1–18 GHz) that were connected to the ports of a vector network analyzer (Agilent E8362C). The polarization is along y direction. The transmitting antenna and the single scatter have been fixed, whereas the receiving antenna was moving around the scatter in the xz plane. The scattering cross-section patterns measured in the xz plane at two distinct frequencies $f = 6.8$ GHz and $f = 9.2$ GHz are plotted in Fig. 6(a) and they are compared with the results of numerical simulations. We find the best agreement for slightly shifted frequencies $f = 6.4$ GHz and $f = 9.0$ GHz, and the difference between the measured Mie resonant frequencies and simulated resonances can be explained by the tolerance of the antenna prototype fabrication. These results clearly demonstrate the multifrequency directional scattering supported by a single dielectric bar scatter.

Next, we consider all-dielectric metasurfaces composed of the elongated bars. A photograph of the experimental metasurface prototype is shown in Fig. 6(b). The transmission and reflection spectra of the metasurface have been investigated both numerically and experimentally. We observe that the metasurface exhibits an expected multimode response with two pronounced maxima in the transmission coefficient (at the frequencies around 6.5 and 9.5 GHz) and one well-defined peak in the reflection coefficient (in the frequency band 7.5–8 GHz), as predicted numerically for the optical frequency range. The slight disagreement between the measured and simulated results in the positions of frequencies in the transmission/reflection maxima and minima can be explained by the tolerance of the sample fabrication. The mismatching in the magnitudes of transmission/reflection coefficients is due to a deviation of permittivity in each particular unit cell caused by different density of ceramic powder.

V. CONCLUSION

We have presented all-dielectric metasurfaces with multimode directionality. Such metasurfaces can support all four possible quadrants of electromagnetic responses and can also work efficiently with either high reflection or high transmission, which may find many applications and largely extends the possibilities of planar optics. We have also demonstrated that this unique multimode property originates from the hybrid Mie-Fabry-Perot modes supported by high-index dielectric structures with large aspect ratios. The revealed hybrid modes and associated multiple magnetic dipole resonances also open a way for engineering the properties of resonant nanostructures and metamaterials.

We also believe that the phenomenon of multimode magnetic dipole moments is responsible for the best efficiency of broadband all-dielectric metasurfaces based on the generalized Huygens principle. Indeed, the superposition of the scattering contributions from several electric and magnetic multipole modes of the constituent meta-atoms allows one to achieve destructive interference in reflection over a large spectral bandwidth, demonstrating reflectionless half-wave plates, quarter-wave plates, and vector beam *q* plates that can operate across multiple telecom bands with ∼99% polarization conversion efficiency [31].

ACKNOWLEDGMENTS

Y.Y. and M.Q. acknowledge financial support from the National Natural Science Foundation of China (Grants No. 61425023, No. 61575177, No. 61275030, and No. 61235007). A.E.M. and Y.S.K. were supported by the Australian Research Council. S.V.K. acknowledges support by the U.S. National Science Foundation under Grant No. 1515343 and by the Department of Defense through the NDSEG program. The numerical simulation and experimental investigation of the metasurfaces in microwave frequency range were supported by the Russian Science Foundation (Project No. 15-12-20028). P.K. acknowledges support from the scholarship of the President of Russian Federation.

APPENDIX A: MULTIPOLE DECOMPOSITION

We employed the Cartesian multipole expansion technique [14,36] to analyze different multipole modes inside the nanobars. The multipoles are calculated through the light-induced polarization $\mathbf{P} = \epsilon_0(\epsilon_r - 1)\mathbf{E}$, where ϵ_0 and ϵ_r are the vacuum permittivity and relative permittivity of the nanobar, respectively. We can write $\mathbf{P}$ as

$$\mathbf{P}(\mathbf{r}) = \int \mathbf{P}(\mathbf{r}')\delta(\mathbf{r} - \mathbf{r}')d\mathbf{r}', \tag{A1}$$

and then expand the delta function in a Talyor series with respect to $\mathbf{r}'$ around the nanobar's center (origin point $\mathbf{r_0}$). Then we can get

$$\mathbf{P}(\mathbf{r}) \simeq \mathbf{p}\delta(\mathbf{r}) + \frac{i}{\omega}[\nabla \times \mathbf{m}\delta(\mathbf{r})] - \frac{1}{6}\hat{Q}\nabla\delta(\mathbf{r}) - \frac{i}{2\omega}[\nabla \times \hat{M}\nabla\delta(\mathbf{r})], \tag{A2}$$

where the multipole moments (electric dipole $\mathbf{p}$, magnetic dipole $\mathbf{m}$, electric quadrupole tensor $\hat{Q}$, and magnetic quadrupole tensor $\hat{M}$) are defined as

$$\mathbf{p} = \int \mathbf{P}(\mathbf{r}')d\mathbf{r}', \tag{A3}$$

$$\mathbf{m} = -\frac{i\omega}{2}\int [\mathbf{r}' \times \mathbf{P}(\mathbf{r}')]d\mathbf{r}', \tag{A4}$$

$$\hat{Q} = 3\int \mathbf{r}'\mathbf{P}(\mathbf{r}') + \mathbf{P}(\mathbf{r}')\mathbf{r}' - \frac{2}{3}[\mathbf{r}' \cdot \mathbf{P}(\mathbf{r}')]\hat{U}d\mathbf{r}', \tag{A5}$$

$$\hat{M} = \frac{\omega}{3i}\int \{[\mathbf{r}' \times \mathbf{P}(\mathbf{r}')]\mathbf{r}' + \mathbf{r}'[\mathbf{r}' \times \mathbf{P}(\mathbf{r}')]\}d\mathbf{r}', \tag{A6}$$

where ω is the angular frequency and $\hat{U}$ is the 3×3 unit tensor. The scattered far-field electric field thus can be calculated by

$$\mathbf{E}_{\text{sca}}(\mathbf{r}) \simeq \frac{k_0^2}{4\pi\epsilon_0}\frac{e^{ik_0 r}}{r}\bigg\{[\mathbf{n} \times [\mathbf{p} \times \mathbf{n}]] + \frac{1}{c}[\mathbf{m} \times \mathbf{n}] + \frac{ik_0}{6}[\mathbf{n}\times[\mathbf{n} \times \hat{Q}\mathbf{n}]] + \frac{ik_0}{2c}[\mathbf{n} \times (\hat{M}\mathbf{n})]\bigg\}, \tag{A7}$$

in which $r = |\mathbf{r}|$, $\mathbf{n}$ is the unit vector directed along $\mathbf{r}$, k_0 is the wave number, and c is the speed of light in a vacuum. The total radiation power P_{sca} of the multipoles is

$$P_{\text{sca}} \simeq \frac{c^2k_0^4Z_0}{12\pi}|\mathbf{p}|^2 + \frac{k_0^4Z_0}{12\pi}|\mathbf{m}|^2 + \frac{c^2k_0^6Z_0}{1440\pi}\sum|Q_{\alpha\beta}|^2 + \frac{k_0^6Z_0}{160\pi}\sum|M_{\alpha\beta}|^2, \tag{A8}$$

where Z_0 is the vacuum wave impedance and $\alpha,\beta \equiv x,y,z$ denote Cartesian components.

APPENDIX B: FIELD DECOMPOSITION OF A DIELECTRIC RESONATOR: THEORY VS SIMULATIONS

Herein we present a theoretical interpretation of the near-field profiles of the hybrid Mie-Fabry-Perot modes. The optical resonances of a dielectric rectangular particle can be described in terms of induced standing waves inside a high impedance cavity. Consider a homogeneous, isotropic dielectric rectangular resonator spanning $x = -W/2$ to $x = W/2$, $y = -L_y/2$ to $y = L_y/2$, and $z = -L_z/2$ to $z = L_z/2$. To decompose the electric and magnetic fields into standing-wave cavity modes we begin with the vector Helmholtz equation, which can be obtained from the source-free Maxwell equations:

$$\nabla \times \nabla \times \{E,H\} - \omega^2 \mu\varepsilon \{E,H\} = 0. \tag{B1}$$

Solution of the vector Helmholtz equation (B1) can be obtained via the rectilinear generating function ψ,

$$\nabla^2 \psi + k^2 \psi = 0, \tag{B2}$$

where $k^2 = \omega^2 \mu\varepsilon$. By separation of variables, the rectilinear generating function may be written as $\psi = X(x)Y(y)Z(z)$. Inserting this into the scalar Helmholtz equation (B2) and dividing by $X(x)Y(y)Z(z)$ yields

$$\frac{1}{X}\frac{\partial^2 X}{\partial x^2} + \frac{1}{Y}\frac{\partial^2 Y}{\partial y^2} + \frac{1}{Z}\frac{\partial^2 Z}{\partial z^2} = -k^2, \tag{B3}$$

from which we deduce

$$\frac{1}{X}\frac{\partial^2 X}{\partial x^2} + k_x^2 X = 0,\ \frac{1}{Y}\frac{\partial^2 Y}{\partial y^2} + k_y^2 Y = 0,\ \frac{1}{Z}\frac{\partial^2 Z}{\partial z^2} + k_z^2 Z = 0, \tag{B4}$$

with $k^2 = k_x^2 + k_y^2 + k_z^2$. The general solution of Eq. (B3) can be written in the following form:

$$\begin{aligned} X &= X_e \cos(k_x x) + X_o \sin(k_x x), \\ Y &= Y_e \cos(k_y y) + Y_o \sin(k_y y), \\ Z &= Z_e \cos(k_z z) + Z_o \sin(k_z z), \end{aligned} \tag{B5}$$

where the corresponding amplitudes are found from the corresponding boundary conditions. For high refractive index particles, due to their high impedance for the wave inside the cavity, perfect magnetic conductors (PMCs) are typically used as approximate boundary conditions [37–39]. PMC boundary conditions are dual to the perfect electric conductor (PEC) conditions used for metallic cavities. Using PMC boundary conditions, i.e., $B_\parallel = E_\perp = 0$, we can deduce the following electric and magnetic field profiles of the cavity modes:

$$\begin{pmatrix} E_x \\ E_y \\ E_z \end{pmatrix} = \begin{pmatrix} A \sin(k_x x)\cos(k_y y)\cos(k_z z) \\ B \cos(k_x x)\sin(k_y y)\cos(k_z z) \\ C \cos(k_x x)\cos(k_y y)\sin(k_z z) \end{pmatrix},$$

$$\begin{pmatrix} B_x \\ B_y \\ B_z \end{pmatrix} = \frac{i}{\omega}\begin{pmatrix} (Ck_y - Bk_z)\cos(k_x x)\sin(k_y y)\sin(k_z z) \\ (Ak_z - Ck_x)\sin(k_x x)\cos(k_y y)\sin(k_z z) \\ (Bk_x - Ak_y)\sin(k_x x)\sin(k_y y)\cos(k_z z) \end{pmatrix}. \tag{B6}$$

Note that magnetic field satisfies the equation $\nabla \cdot B = 0$. The coefficients A,B,C are subject to the condition $\nabla \cdot E = 0$, which leads to the condition $Ak_x + Bk_y + Ck_z = 0$. The boundary conditions determine the eigenfrequency of the cavity modes as

$$\begin{aligned} f &= \frac{\omega}{2\pi} = \frac{ck}{2\pi\sqrt{\varepsilon\mu}} = \frac{c}{2\pi\sqrt{\varepsilon\mu}}\sqrt{k_x^2 + k_y^2 + k_z^2} \\ &= \frac{c}{2\pi\sqrt{\varepsilon\mu}}\sqrt{\left(\frac{n\pi}{W}\right)^2 + \left(\frac{m\pi}{L_y}\right)^2 + \left(\frac{l\pi}{L_z}\right)^2}, \\ f_{nml} &= \frac{c}{2\sqrt{\varepsilon\mu}}\sqrt{\left(\frac{n}{W}\right)^2 + \left(\frac{m}{L_y}\right)^2 + \left(\frac{l}{L_z}\right)^2}, \end{aligned} \tag{B7}$$

with $k_x = \frac{n\pi}{W}$, $k_y = \frac{m\pi}{L_y}$, $k_x = \frac{l\pi}{L_z}$. It should be noted that Eq. (B7) holds both for dielectric and metallic cavities because of the duality of PEC and PMC conditions, whereas the electric and magnetic fields obtained in Eq. (B6) for dielectric resonators are distinct from those for metallic cavities [40]. To relate this mode analysis to the scattering problem, we fix the direction of propagation along the z axis. For TM modes $B_z = 0$, which requires that $Bk_x - Ak_y = 0$, or $B = \frac{k_y}{k_x}A$ and $C = -\frac{A}{k_z}(\frac{k_y^2}{k_x} + k_x)$. This yields the E and B fields for TM_{nml} modes:

$$\begin{pmatrix} E_x \\ E_y \\ E_z \end{pmatrix} = A\begin{pmatrix} \sin\left(\frac{n\pi}{W}x\right)\cos\left(\frac{m\pi}{L_y}y\right)\cos\left(\frac{l\pi}{L_z}z\right) \\ \frac{mW}{nL_y}\cos\left(\frac{n\pi}{W}x\right)\sin\left(\frac{m\pi}{L_y}y\right)\cos\left(\frac{l\pi}{L_z}z\right) \\ -\frac{L_z(n^2L_y^2+m^2W^2)}{nlWL_y^2}\cos\left(\frac{n\pi}{W}x\right)\cos\left(\frac{m\pi}{L_y}y\right)\sin\left(\frac{l\pi}{L_z}z\right) \end{pmatrix},$$

$$\begin{pmatrix} B_x \\ B_y \\ B_z \end{pmatrix} = \frac{iA}{\omega}\begin{pmatrix} -(\frac{mL_z(n^2L_y^2+m^2W^2)}{nlWL_y^3} + \frac{mlW}{nL_yL_z})\cos\left(\frac{n\pi}{W}x\right)\sin\left(\frac{m\pi}{L_y}y\right)\sin\left(\frac{l\pi}{L_z}z\right) \\ (\frac{L_z(n^2L_y^2+m^2W^2)}{lW^2L_y^2} + \frac{l}{L_z})\sin\left(\frac{n\pi}{W}x\right)\cos\left(\frac{m\pi}{L_y}y\right)\sin\left(\frac{l\pi}{L_z}z\right) \\ 0 \end{pmatrix}. \tag{B8}$$

The cavity modes TM_{101} and TM_{301} [see Figs. 7(a) and 7(b)] replicate the electromagnetic field structure of two magnetic dipolar resonances in Fig. 3 (see main text). One might also construct higher-order magnetic dipole mode profiles for larger values of $n > 1$ and $l > 1$ [see Figs. 7(c) and 7(d)] and corresponding scattering resonant modes in Figs. 8 and 9. We would like to emphasize that this theoretical treatment is based on the approximate PMC boundary conditions which are only applicable to high-permittivity structures. There is no exact closed-form expression available for the resonant frequencies

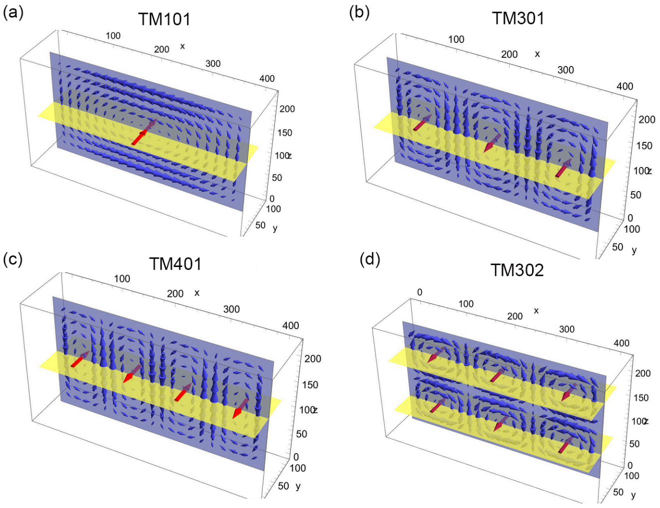

FIG. 7. Profile of the resonant cavity modes. Typical TM modes of the rectilinear cavity with quantum numbers (a) $n=1$, $m=0$, $l=1$; (b) $n=3$, $m=0$, $l=1$; (c) $n=4$, $m=0$, $l=1$; and (d) $n=3$, $m=0$, $l=2$. The blue arrows indicate electric vector field and the red arrows indicate magnetic vector field. The TM_{101} and TM_{301} modes replicate the field distribution of two magnetic dipole modes in Fig. 3 in the main text.

or field distributions of such dielectric resonators, but we have provided an approximate solution to extract the essential modal behavior seen in simulations, as discussed in the main text.

APPENDIX C: RADIATION OF MD_2 MODES

It is worth noting that for the conventional multipole decomposition, the MD mode is usually defined as only one magnetic dipole positioned in the center of the particle [Eq. (A4)]. However, here we can observe two separate magnetic dipoles in the near-field distributions of the MD_2 mode (the magnetic dipole in the center is neglected since simulations show it to be weak) [Fig. 3(c)]. Usually two dipoles cannot be equivalently replaced by one dipole because the spatial distance between the two dipoles can lead to an additional phase term in the far-field response. However, in the following, we will show that Eq. (A4) and conventional multipole decomposition are still valid for the MD_2 mode and can clearly reveal its underlying physics.

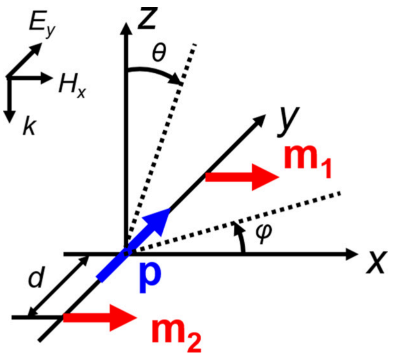

FIG. 8. Equivalent model for second magnetic resonance.

First we consider two separate magnetic dipoles $\mathbf{m_1}$ and $\mathbf{m_2}$ at the MD_2 resonance with a spatial distance $2d$, as shown in Fig. 8.

Given the axial symmetry of the structure, we can assume that these two magnetic dipoles are identical to each other with $\mathbf{m}_j = \frac{1}{2}\mathbf{m}_{\mathrm{MD2}}$ $(j=1,2)$, where $\mathbf{m}_{\mathrm{MD2}}$ is the total magnetic dipole moment that we can obtain through the multipole expansion. We note $\mathbf{y}_j$ the position vectors of the two magnetic dipoles and thus we can write the electric field $\mathbf{E}_\mathrm{m}$ produced in the far field by these two magnetic dipoles as

$$\mathbf{E}_\mathrm{m}(\mathbf{r}) = \sum_j \frac{k_0^2}{4\pi\epsilon_0 rc} e^{ik|\mathbf{r}-\mathbf{y}_j|}(\mathbf{m}_j \times \mathbf{n}). \tag{C1}$$

At far-field limit where $r \gg d$ we can have

$$\begin{aligned}|\mathbf{r}-\mathbf{y}_j| - r &= \sqrt{x^2+(y\mp d)^2+z^2} - r \\ &\approx r\left(\sqrt{1\mp\frac{2yd}{r^2}} - 1\right) \\ &\approx \mp d\left(\frac{y}{r}\right) \approx \mp d\sin\theta\sin\varphi. \end{aligned} \tag{C2}$$

Then we can derive $\mathbf{E}_\mathrm{m}$ as follows:

$$\begin{aligned}\mathbf{E}_\mathrm{m} &= \frac{k_0^2}{4\pi\epsilon_0 c}|\mathbf{m}_{\mathrm{MD2}}|\frac{e^{ikr}}{r}\cos(kd\sin\theta\sin\varphi) \\ &\quad \times(-\sin\varphi\hat{\boldsymbol{\theta}} + \cos\theta\cos\varphi\hat{\boldsymbol{\varphi}}). \end{aligned} \tag{C3}$$

with $\hat{\boldsymbol{\theta}}$ and $\hat{\boldsymbol{\varphi}}$ the unit vectors of the spherical basis. In the above equation, one can clearly see the additional term $\cos(kd\sin\theta\sin\varphi)$ contributed by the spatial distance and how it influences the far-field response. However, this additional term will not have an impact on the total scattered power P_m contributed by the two magnetic dipoles, which can be determined by the following expression:

$$\begin{aligned}P_m &= \int_\Omega dP_m d\Omega = \frac{1}{2Z_0}\int_0^\pi\int_0^{2\pi}|\mathbf{E}_\mathrm{m}|^2 r^2 \sin\theta d\theta d\varphi \\ &= \frac{Z_0 k^4}{12\pi}|\mathbf{m}_{\mathrm{MD2}}|^2. \end{aligned} \tag{C4}$$

Equation (C4) shows that the power contribution P_m of two separate identical magnetic dipoles is only determined by their total magnetic dipole moment other than their relative positions. In our paper, we decompose the far-field scattering cross section into multipolar series, which is only related to the power contribution of each multipole. Therefore, the second peak in the MD curve represents a local maximum contribution from the MD modes to the total scattering power, proving the existence of the MD_2 mode which consists of two magnetic dipoles.

Next, we consider the interference of the MD_2 and ED mode. As shown in Fig. 8, there is also an induced electric dipole $\mathbf{p}$ oscillating along y direction. One can write the total electric field $\mathbf{E}_{\mathrm{pm}}$ induced by the three dipoles as

$$\begin{aligned}\mathbf{E}_{\mathrm{pm}}(\mathbf{r}) &= \frac{k_0^2}{4\pi\epsilon_0 r}e^{ikr}\Big[|\mathbf{p}|(\cos\theta\sin\varphi\hat{\boldsymbol{\theta}} - \cos\varphi\hat{\boldsymbol{\varphi}}) \\ &\quad + 2\frac{|\mathbf{m}_j|}{c}\cos(kd\sin\theta\sin\varphi)(-\sin\varphi\hat{\boldsymbol{\theta}} + \cos\theta\cos\varphi\hat{\boldsymbol{\varphi}})\Big]. \end{aligned} \tag{C5}$$

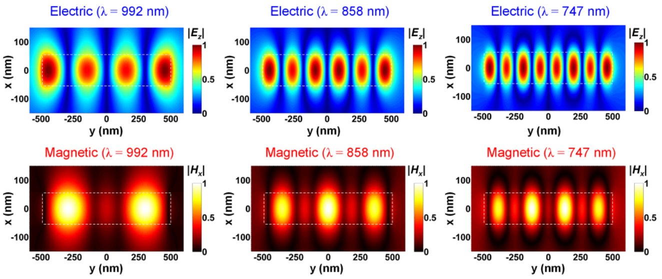

FIG. 9. Near-field distributions of electric and magnetic fields of the nanobar with $L_y = 1000$ nm, $W = 110$ nm, and $L_z = 220$ nm.

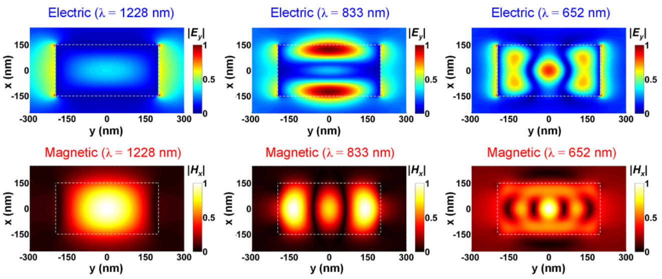

FIG. 10. Near-field distributions of electric and magnetic fields of the nanobar with $W = 300$ nm, $L_y = 400$ nm, and $L_z = 220$ nm.

Given the incident light is along $-z$ direction in our study, the backward and forward radar cross sections of the nanobar can be defined as

$$\begin{aligned}\sigma_{\text{back}} &= \lim_{r\to\infty} 4\pi r^2 \frac{|\mathbf{E}_{\text{pm}}(\theta = 0,\varphi = 0)|^2}{|\mathbf{E}_{\text{inc}}|^2}\\ &= \frac{k^4}{4\pi\epsilon_0|\mathbf{E}_{\text{inc}}|^2}\left|p_y - 2\frac{m_{xj}}{c}\right|^2, \qquad \text{(C6)}\end{aligned}$$

$$\begin{aligned}\sigma_{\text{forward}} &= \lim_{r\to\infty} 4\pi r^2 \frac{|\mathbf{E}_{\text{pm}}(\theta = \pi,\varphi = 0)|^2}{|\mathbf{E}_{\text{inc}}|^2}\\ &= \frac{k^4}{4\pi\epsilon_0|\mathbf{E}_{\text{inc}}|^2}\left|p_y + 2\frac{m_{xj}}{c}\right|^2, \qquad \text{(C7)}\end{aligned}$$

with $|\mathbf{E}_{\text{inc}}|$ the amplitude of the incident electric field, and $|p_y|$ and $|m_{xj}|$ the amplitudes of the induced electric and magnetic dipole moments. Therefore, suppressed backscattering and maximum forward scattering occur if the condition

$$p_y = \frac{2}{c}m_{xj} = \frac{1}{c}m_{\text{MD2}} \qquad \text{(C8)}$$

is satisfied. Equation (C8) clearly reveals that, for a system consisting of ED and MD_2 modes, unidirectional forward scattering can only appear when the electric dipole moment p is equal to the total dipole moment m_{MD2} of the two magnetic dipoles m_j. When there is only one fundamental magnetic dipole, Eq. (C8) becomes $p_y = \frac{1}{c}m_x$, which is the well-known first Kerker condition [27].

APPENDIX D: NEAR-FIELD DISTRIBUTIONS OF HIGHER-ORDER HYBRID MODES

As predicted by the theory (Fig. 7) and demonstrated by the numerical simulations (Fig. 4), we expect to find higher-order hybrid modes accompanied by higher-order multipoles and cavity modes with increasing geometric parameters. Here we show their near-field distributions.

For increased length $L_y = 1000$ nm (Fig. 9), to clearly illustrate the "higher-mode" magnetic dipolar responses and the associated higher-order cavity modes, here we plot field components E_z and H_x. It can be readily seen that the three peaks ($\lambda = 992$, 858, and 747 nm) in the scattering spectrum [see Fig. 4(c)] correspond to the existence of the MD_2, MD_3, and MD_4 modes, respectively.

For increased width $W = 300$ nm (Fig. 10), fundamental ED and MD modes can be clearly seen at $\lambda = 1228$ nm, while at $\lambda = 833$ nm, an ED_2 mode accompanied by a standing-wave pattern (three antinodes) in x direction can be observed. A MD_2 mode can also be seen at this wavelength. For shorter wavelength $\lambda = 652$ nm, we observe complex and hybrid modal distributions while the higher-mode ED and MD responses could still be distinguished.

---

[1] L. Novotny and B. Hecht, *Principles of Nano-Optics* (Cambridge University Press, Cambridge, UK, 2012).
[2] J. A. Schuller, E. S. Barnard, W. Cai, Y. C. Jun, J. S. White, and M. L. Brongersma, Plasmonics for extreme light concentration and manipulation, Nat. Mater. **9**, 193 (2010).
[3] L. Novotny and N. Van Hulst, Antennas for light, Nat. Photonics **5**, 83 (2011).
[4] A. Kinkhabwala, Z. Yu, S. Fan, Y. Avlasevich, K. Müllen, and W. E. Moerner, Large single-molecule fluorescence enhancements produced by a bowtie nanoantenna, Nat. Photonics **3**, 654 (2009).
[5] A. G. Curto, G. Volpe, T. H. Taminiau, M. P. Kreuzer, R. Quidant, and N. F. van Hulst, Unidirectional emission of a quantum dot coupled to a nanoantenna, Science **329**, 930 (2010).
[6] D. K. Gramotnev and S. I. Bozhevolnyi, Plasmonics beyond the diffraction limit, Nat. Photonics **4**, 83 (2010).
[7] A. V. Kildishev, A. Boltasseva, and V. M. Shalaev, Planar photonics with metasurfaces, Science **339**, 1232009 (2013).
[8] N. I. Zheludev and Y. S Kivshar, From metamaterials to metadevices, Nat. Mater. **11**, 917 (2012).
[9] S. Jahani and Z. Jacob, All-dielectric metamaterials, Nat. Nanotechnol. **11**, 23 (2016).
[10] A. I. Kuznetsov, A. E. Miroshnichenko, M. L. Brongersma, Y. S. Kivshar, and B. Lukyanchuk, Optically resonant dielectric nanostructures, Science **354**, aag2472 (2016).
[11] A. B. Evlyukhin, S. M. Novikov, U. Zywietz, R. L. Eriksen, C. Reinhardt, S. I. Bozhevolnyi, and B. N. Chichkov,

Demonstration of magnetic dipole resonances of dielectric nanospheres in the visible region, Nano Lett. **12**, 3749 (2012).
[12] A. I. Kuznetsov, A. E. Miroshnichenko, Y. H. Fu, J. Zhang, and B. Luk'Yanchuk, Magnetic light, Sci. Rep. **2**, 492 (2012).
[13] A. P. Slobozhanyuk, A. N. Poddubny, A. E. Miroshnichenko, P. A. Belov, and Y. S. Kivshar, Subwavelength Topological Edge States in Optically Resonant Dielectric Structures, Phys. Rev. Lett. **114**, 123901 (2015).
[14] A. E. Miroshnichenko, A. B. Evlyukhin, Y. F. Yu, R. M. Bakker, A. Chipouline, A. I. Kuznetsov, B. Lukyanchuk, B. N. Chichkov, and Y. S. Kivshar, Nonradiating anapole modes in dielectric nanoparticles, Nat. Commun. **6**, 8069 (2015).
[15] I. Staude, A. E. Miroshnichenko, M. Decker, N. T. Fofang, S. Liu, E. Gonzales, J. Dominguez, T. S. Luk, D. N. Neshev, I. Brener, and Y. Kivshar, Tailoring directional scattering through magnetic and electric resonances in subwavelength silicon nanodisks, ACS Nano **7**, 7824 (2013).
[16] B. S. Lukyanchuk, N. V. Voshchinnikov, R. Paniagua-Domínguez, and A. I. Kuznetsov, Optimum forward light scattering by spherical and spheroidal dielectric nanoparticles with high refractive index, ACS Photonics **2**, 993 (2015).
[17] J. C. Ginn, I. Brener, D. W. Peters, J. R. Wendt, J. O. Stevens, P. F. Hines, L. I. Basilio, L. K. Warne, J. F. Ihlefeld, P. G. Clem, and M. B. Sinclair, Realizing Optical Magnetism from Dielectric Metamaterials, Phys. Rev. Lett. **108**, 097402 (2012).
[18] D. Sikdar, W. Cheng, and M. Premaratne, Optically resonant magneto-electric cubic nanoantennas for ultra-directional light scattering, J. Appl. Phys. **117**, 083101 (2015).
[19] K. Vynck, D. Felbacq, E. Centeno, A. I. Căbuz, D. Cassagne, and B. Guizal, All-Dielectric Rod-Type Metamaterials at Optical Frequencies, Phys. Rev. Lett. **102**, 133901 (2009).
[20] P. Fan, Z. Yu, S. Fan, and M. L. Brongersma, Optical Fano resonance of an individual semiconductor nanostructure, Nat. Mater. **13**, 471 (2014).
[21] Y. Yang, Q. Li, and M. Qiu, Controlling the angular radiation of single emitters using dielectric patch nanoantennas, Appl. Phys. Lett. **107**, 031109 (2015).
[22] H.-S. Ee, J.-H. Kang, M. L. Brongersma, and M.-K. Seo, Shape-dependent light scattering properties of subwavelength silicon nanoblocks, Nano Lett. **15**, 1759 (2015).
[23] J. Tian, Q. Li, Y. Yang, and M. Qiu, Tailoring unidirectional angular radiation through multipolar interference in a single-element subwavelength all-dielectric stair-like nanoantenna, Nanoscale **8**, 4047 (2016).
[24] Y. H. Fu, A. I. Kuznetsov, A. E. Miroshnichenko, Y. F. Yu, and B. Lukyanchuk, Directional visible light scattering by silicon nanoparticles, Nat. Commun. **4**, 1527 (2013).
[25] A. E. Krasnok, A. E. Miroshnichenko, P. A. Belov, and Y. S. Kivshar, Huygens optical elements and yagiuda nanoantennas based on dielectric nanoparticles, JETP Lett. **94**, 593 (2011).
[26] S. Liu, M. B. Sinclair, T. S. Mahony, Y. C. Jun, S. Campione, J. Ginn, D. A. Bender, J. R. Wendt, J. F. Ihlefeld, P. G. Clem *et al.*, Optical magnetic mirrors without metals, Optica **1**, 250 (2014).
[27] M. Kerker, D.-S. Wang, and C. L. Giles, Electromagnetic scattering by magnetic spheres, J. Opt. Soc. Am. **73**, 765 (1983).
[28] R. C. Devlin, M. Khorasaninejad, W. T. Chen, J. Oh, and F. Capasso, Broadband high-efficiency dielectric metasurfaces for the visible spectrum, Proc. Natl. Acad. Sci. USA **113**, 10473 (2016).
[29] M. Khorasaninejad, W. T. Chen, J. Oh, and F. Capasso, Super-dispersive off-axis meta-lenses for compact high resolution spectroscopy, Nano Lett. **16**, 3732 (2016).
[30] F. Wang, Q.-H. Wei, and H. Htoon, Generation of steep phase anisotropy with zero-backscattering by arrays of coupled dielectric nano-resonators, Appl. Phys. Lett. **105**, 121112 (2014).
[31] S. Kruk, B. Hopkins, I. Kravchenko, A. Miroshnichenko, D. N. Neshev, and Y. S. Kivshar, Broadband highly-efficient dielectric metadevices for polarization control, APL Photonics **1**, 030801 (2016).
[32] Lumerical Solutions Inc., http://www.lumerical.com/tcad-products/fdtd
[33] E. D. Palik, *Handbook of Optical Constants of Solids* (Academic, New York, 1998), Vol. 3.
[34] D. R. Smith, S. Schultz, P. Markoš, and C. M. Soukoulis, Determination of effective permittivity and permeability of metamaterials from reflection and transmission coefficients, Phys. Rev. B **65**, 195104 (2002).
[35] CST Microwave Studio, http://www.cst.com
[36] A. B. Evlyukhin, C. Reinhardt, E. Evlyukhin, and B. N. Chichkov, Multipole analysis of light scattering by arbitrary-shaped nanoparticles on a plane surface, J. Opt. Soc. Am. B **30**, 2589 (2013).
[37] H. Y. Yee, Natural resonant frequencies of microwave dielectric resonators (correspondence), IEEE Trans. Microwave Theory Tech. **13**, 256 (1965).
[38] A. Okaya and L. F. Barash, The dielectric microwave resonator, Proc. IRE **50**, 2081 (1962).
[39] R. K. Mongia and A. Ittipiboon, Theoretical and experimental investigations on rectangular dielectric resonator antennas, IEEE Trans. Antennas Propag. **45**, 1348 (1997).
[40] C. A. Balanis, *Advanced Engineering Electromagnetics* (Wiley, New York, 2012).